


# Superresolution Diffuse Optical Imaging by Localization of Fluorescence

Brian Z. Bentz,<sup>1,2</sup> Dergan Lin,<sup>2</sup> and Kevin J. Webb<sup>2,\*</sup>

<sup>1</sup>*Sandia National Laboratories, Albuquerque, New Mexico 87123, USA*

<sup>2</sup>*Purdue University, West Lafayette, Indiana 47907, USA*

 (Received 10 January 2018; revised manuscript received 25 May 2018; published 11 September 2018)

The multiple scattering of light presents major challenges in realizing useful *in vivo* imaging at tissue depths of more than about one millimeter, where many answers to health questions lie. Visible through near-infrared photons can be readily and safely detected through centimeters of tissue; however, limited information is available for image formation. One strategy for obtaining images is to model the photon transport and a simple incoherent model is the diffusion equation approximation to the Boltzmann transport equation. Such an approach provides a prediction of the mean intensity of heavily scattered light and hence provides a forward model for optimization-based computational imaging. While diffuse optical imaging methods have received substantial attention, they remain restricted in terms of resolution because of the loss of high-spatial-frequency information that is associated with the multiple scattering of photons. Consequently, only relatively large inhomogeneities, such as tumors or organs in small animals, can be effectively resolved. Here, we introduce a superresolution imaging approach based on point localization in a diffusion framework that enables over two orders of magnitude improvement in the spatial resolution of diffuse optical imaging. The method is demonstrated experimentally by localizing a fluorescent inhomogeneity in a highly scattering slab and characterizing the localization uncertainty. The approach allows imaging through centimeters of tissue with a resolution of tens of microns, thereby enabling cells or cell clusters to be resolved. More generally, this high-resolution imaging approach could be applied with any physical transport or wave model and hence to a broad class of physical problems. Paired with a suitable optical contrast mechanism, as can be realized with targeted fluorescent molecules or genetically modified animals, superresolution diffuse imaging should open alternative dimensions for *in vivo* applications.

DOI: [10.1103/PhysRevApplied.10.034021](https://doi.org/10.1103/PhysRevApplied.10.034021)

## I. INTRODUCTION

The interaction of light with tissue has received intense study due to a myriad of applications in biomedical science [1–3]. Near the tissue surface, coherent methods are used to image with spatial resolutions at the diffraction limit [4]. However, in deep tissue, where the propagation direction of light is randomized due to optical scattering, the formation of an image becomes a much greater challenge. Coherent imaging is still possible, for example, through feedback control of the amplitude and phase of the incident wave front, which has allowed focusing of light to depths of about 1 mm in tissue [5]. Alternatively, the tissue can be characterized through measurement and inversion of a field transmission matrix, allowing image formation [6–8]. These types of coherent methods can achieve high resolution; however, they are generally less effective as the amount of scatter increases, limiting their application in deep (> 1 cm) tissue. Coherent imaging through almost any amount of scatter is possible using speckle-intensity corre-

lations over object position [9,10]. However, this method requires that the positional change of the object is known or can be estimated.

Deep-tissue imaging is achievable with diffuse optical imaging (DOI), a computational imaging method in which a model of light transport in scattering media allows extraction of images from incoherent light [2,3,11,12]. For example, in diffuse optical tomography (DOT) [3,13–15], three-dimensional (3D) images of the spatially dependent optical properties are iteratively reconstructed from boundary measurements of highly scattered light. With the addition of fluorescent contrast agents, fluorescence diffuse optical tomography (FDOT) allows computational imaging of targeted biochemical pathways [16,17]. FDOT has proven especially useful for *in vivo* small animal studies of, for example, targeted drugs [18] and misfolding of protein aggregates [19]. However, the low resolution of DOI methods such as FDOT compared to coherent methods [20] has restricted the applications.

Here, we present a method to circumvent previous DOI resolution limits. We use optical localization, where information about the location of the centroid

\*webb@purdue.edu

of an inhomogeneity is extracted. We call the method superresolution diffuse optical imaging (SRDOI). The case we consider is a small region embedded in a heavily scattering background that contains fluorophores. Multiple fluorescent regions could be similarly imaged at high resolution when the emission from each region is separable, for example, through sufficient spatial, temporal, or spectral separation, or a combination of these. The results indicate that by localizing many inhomogeneities individually within a highly scattering medium and combining the positions into a single image, high-resolution DOI can be achieved.

Previous studies have localized fluorescent inhomogeneities in deep tissue [21–24]. For example, boundary measurements of fluorescence emission have allowed extraction of the location of fluorescing tumors [23,25]. In these studies, tumor masses were localized after injecting mice with fluorescent contrast agents that targeted specific cancer cells. However, the implications and limits for high-resolution imaging have not been previously examined.

In Sec. II, the diffusion model for light propagation is described and the spatial resolution that has been achieved by DOI in the literature is considered, as a comparison for SRDOI. In Sec. III, the fluorescent localization method is presented, including the derivation of the forward model and the optimization procedure. In Sec. IV, the performance of SRDOI is characterized with numerical simulation and experimental validation in a slab geometry. The SRDOI results demonstrate two orders of magnitude improvement in the spatial resolution compared to FDOT.

## II. DIFFUSE OPTICAL IMAGING

Optical transport in tissue can be described by the radiative transfer equation, and under restrictions on scattering strength (weak), absorption (weak), and time (long compared to the scattering time), and with sufficient scatter, the diffusion approximation provides a simple model [3,13]. In the frequency domain, the light source is modulated at angular frequency  $\omega$ , i.e., we assume  $\exp(-i\omega t)$  variation. For a fluorescence source in a locally homogeneous medium, the coupled diffusion equations can then be written in the form of wave equations as [17]

$$\nabla^2 \phi_x(\mathbf{r}) + k_x^2 \phi_x(\mathbf{r}) = -S_x(\mathbf{r}), \quad (1)$$

$$\nabla^2 \phi_m(\mathbf{r}) + k_m^2 \phi_m(\mathbf{r}) = -\phi_x(\mathbf{r})S_f(\mathbf{r}), \quad (2)$$

where  $\mathbf{r}$  denotes position;  $\phi$  (W/mm<sup>2</sup>) is the photon flux density; the subscripts  $x$  and  $m$ , respectively, denote parameters at the fluorophore excitation and emission wavelengths,  $\lambda_x$  and  $\lambda_m$ ;  $k^2 = -\mu_a/D + i\omega/(Dv)$ , where  $D = 1/[3(\mu'_s + \mu_a)]$  (mm) is the diffusion coefficient;  $\mu'_s$  is the

reduced scattering coefficient;  $\mu_a$  is the absorption coefficient;  $v$  is the speed of light within the medium;  $S_x(\mathbf{r})$  is the excitation source; and  $S_f(\mathbf{r})$  describes the fluorescence emission. In an infinite homogeneous space, the frequency-domain diffusion equation (written as a lossy wave equation) Green's function is

$$g(\mathbf{r}', \mathbf{r}) = \frac{e^{ik|\mathbf{r}-\mathbf{r}'|}}{4\pi|\mathbf{r}-\mathbf{r}'|}, \quad (3)$$

where  $\mathbf{r}'$  is the position of a point source and the complex wave number  $k$  is applied at  $\lambda_x$  or  $\lambda_m$  in Eqs. (1) or (2), respectively.

Solutions to Eqs. (1) and (2) are called diffuse photon density waves (DPDWs) [2,26,27]. Here, we refer to data formed through experimental detection of DPDWs as measurements. In Sec. III A, we derive a forward model using Eqs. (1) and (2), which we treat as an estimate of the expected values of the measurements. In contrast, images recovered using an inversion method (an indirect imaging method that extracts desired parameters (e.g.,  $\mathbf{r}'$ ) from measurement data (e.g.,  $\phi$ ) through inversion of a forward model) are referred to as reconstructed images. The resolution of a reconstructed image depends on the method used (see, e.g., Refs. [28,29]). Of note, the treatment of the nonlinear nature of the inversion process and the use of constraints (or a prior model in a Bayesian sense) can be of substantial consequence.

Even without absorption, the DPDW wavenumber is complex, implying that there are always both propagation and attenuation at any spatial frequency [27]. The wavelength of DPDWs for typical tissue and modulation frequencies (10 MHz or so) is on the order of a few centimeters. Measurements are therefore usually made within distances less than about one wavelength from a source location, placing them in the near field in this sense. However, the attenuation of high spatial frequencies is still severe, causing a significant reduction in resolution with depth. Here, we define resolution as the full width at half maximum (FWHM) of the point-spread function (PSF), where the PSF is the image of a point source located in the scattering medium. Equivalently, the resolution is the distance between two identical point sources such that their PSFs intersect at their FWHM.

The dependence of the resolution on depth is nonlinear and has been estimated using the FWHM of the propagation transfer function in a homogeneous infinite medium [27]. The resolution is unrelated to the diffraction limit because DPDWs have a complex wavenumber and are measured in the near field. The resolution depends primarily on  $\mu'_s$ ,  $\mu_a$ , and the distance from the source to detectors. In practice, however, the resolution depends on many other factors, including the measurement signal-to-noise ratio (SNR), the medium geometry, the source-detector diversity, the contrast between the inhomogeneity and the

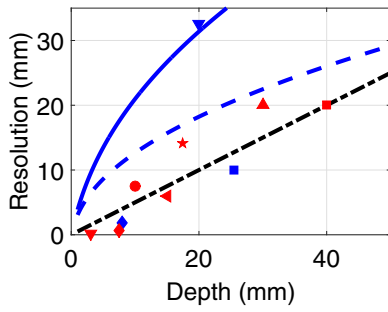


FIG. 1. The resolution of diffuse optical imaging as reported in the literature. Red symbols are image reconstructions, where  $\blacktriangledown$ ,  $\blacklozenge$ ,  $\bullet$ ,  $\blacktriangleleft$ ,  $\star$ ,  $\blacktriangle$ , and  $\blacksquare$  correspond to Refs. [28–34]. Blue symbols are direct measurements (no inversion performed), where  $\blacklozenge$ ,  $\blacktriangledown$ , and  $\blacksquare$  correspond to Refs. [35–37]. The background  $\mu'_s$  and  $\mu_a$  used in each paper vary, but their average values are 0.85 and 0.0063  $\text{mm}^{-1}$  (close to those of tissue-simulating Intralipid), where  $\mu'_s$  is between 0.5 and 1.0  $\text{mm}^{-1}$  and  $\mu_a$  is between 0 and 0.01  $\text{mm}^{-1}$ . The blue curves are theoretical resolution limits for continuous wave (CW) ( $\omega = 0$ ) direct measurements, as calculated by Ripoll *et al.* [27]. The dashed blue curve is calculated using breast-tissue parameters, where  $\mu'_s = 1.5 \text{ mm}^{-1}$  and  $\mu_a = 0.0035 \text{ mm}^{-1}$ . The solid blue curve is calculated using the average values from the literature. The black long-short-dashed curve is half the depth.

background, and the experimental setup. For the case of reconstructed images, the resolution will also depend on the computational method used for reconstruction.

As a comparison for the work presented here, Fig. 1 shows a plot of the resolutions achieved based on both measured data (without reconstruction of an image) and image reconstructions (through a computational imaging procedure). The red symbols are reconstructed image resolutions (without prior information) and the blue symbols are direct measurement resolutions. The blue curves are analytic resolution limits of direct measurements for  $\mu'_s$  and  $\mu_a$  typical of tissue, as calculated by Ripoll *et al.* [27]. From Fig. 1, we find that for optical properties similar to tissue and beyond a depth of about 1 cm, the reported reconstructed image resolution is typically about half the depth, as represented by the dashed black line.

The resolution in Fig. 1 can be improved with the incorporation of prior information that constrains the inverse problem. When combined with other imaging modalities, such as MRI [38,39], the resolution can be improved to that of the higher-resolution method. Here, we show that the resolution of DOI can be greatly improved through localization, where the problem becomes one of finding the position of a point source [21–23]. The prior information that is incorporated into the inversion is that a measurement data set contains information about only a single fluorescent inhomogeneity. In practice, such measurements could be made, for example, if the inhomogeneities have sufficient separation in space, time, and/or emission spectrum. Furthermore, we model every inhomogeneity as

a point source, an assumption that has been shown to be valid numerically and experimentally for fluorescent inhomogeneities with diameters up to 10 mm at depths of 10–20 mm in tissue-simulating 1% Intralipid [23]. This assumption holds because of the rapid attenuation of high spatial frequencies within the scattering medium. Here, the efficacy of localizing a cylindrical fluorescent inhomogeneity with 1 mm diameter and 2 mm height is demonstrated. With sufficient SNR, smaller inhomogeneities could be localized and previous work [23] suggests that larger inhomogeneities with diameters of at least 10 mm could also be localized. If needed, the forward model could be modified for structured or larger inhomogeneities [40], extending localization beyond a single point in space.

### III. LOCALIZATION FOR SUPERRESOLUTION

We propose localization as a means for finding fluorescent inhomogeneities embedded within a highly scattering medium with great precision. The method estimates the location of an inhomogeneity by fitting measured intensity data to a diffusion equation forward model for a point emitter, allowing extraction of the 3D position of the inhomogeneity. For the forward model, we use an analytic solution to the diffusion equation in an infinite slab geometry [1] and we note that analytic solutions can be derived for more complicated geometries [41], or the forward model could be solved using a numerical method [42].

#### A. The forward model

Equations (1) and (2) can be used to derive a forward model for comparison with measured data. For experimental simplicity, we set  $\omega = 0$ , so that the data are an integration over the measured temporal response at each measurement location. As seen in Fig. 2, a single point-excitation source corresponding to the laser excitation is positioned at  $\mathbf{r}_s$ . In this case,  $S_x(\mathbf{r}) = S_o \delta(\mathbf{r} - \mathbf{r}_s)$ , where  $S_o$  is the laser-excitation power density ( $\text{W}/\text{mm}^3$ ) and  $\delta$  is the Dirac delta function. Furthermore,  $N$  point detectors at  $\lambda_m$  that correspond to camera pixels behind an emission bandpass filter are placed at positions  $\mathbf{r}_i$ , where  $i$  is an index from 1 to  $N$ . Finally, in the example we consider, a single fluorescent point source is located at  $\mathbf{r}_f$ , such that  $S_f(\mathbf{r}) = \eta \mu_{a_f} \delta(\mathbf{r} - \mathbf{r}_f)$ , where  $\eta$  is the fluorophore's quantum yield and  $\mu_{a_f}$  is its absorption. The estimation of  $\mathbf{r}_f$  constitutes localization. Under these conditions, we let  $g_x(\mathbf{r}_s, \mathbf{r}_f)$  represent the Green's function for Eq. (1) at  $\lambda_x$  (the excitation wavelength) and we let  $g_m(\mathbf{r}_f, \mathbf{r}_i)$  be the Green's function for Eq. (2) at  $\lambda_m$  (the emission wavelength), assuming an infinite slab geometry. Then, the  $i$ th element of the forward model vector, describing the fluorescence emission

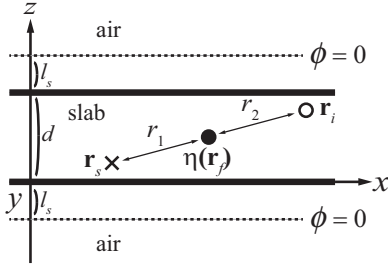


FIG. 2. The model geometry for an infinite slab of thickness  $d$ , where  $\mathbf{r} = (x, y, z)$  and the  $y$  axis is going into the page. An excitation source (X) at  $\mathbf{r}_s$  and a fluorescence-emission detector (O) at  $\mathbf{r}_i$  are placed one mean-free-path length,  $l^* = 3D$ , away from the slab boundaries, as shown. A fluorescence inhomogeneity (●) is at the unknown position  $\mathbf{r}_f$ . Zero-flux ( $\phi = 0$ ) boundary conditions with  $l_s = 5.03D$  are used to simulate an infinite slab geometry [23].

measured at  $\mathbf{r}_i, \tilde{f}_i$ , is

$$\tilde{f}_i(\mathbf{r}_f) = w[g_m(\mathbf{r}_f, \mathbf{r}_i)g_x(\mathbf{r}_s, \mathbf{r}_f)], \quad (4)$$

$$\equiv wf_i(\mathbf{r}_f), \quad (5)$$

where  $w$  is a multiplicative constant that incorporates  $\eta, S_o$ , and the efficiency of light coupling into the medium, and  $f_i(\mathbf{r}_f)$  depends nonlinearly on  $\mathbf{r}_f$ . The excitation laser light incident upon the medium is approximated in the model as an isotropic point source located one mean-free-path length ( $l^* = 3D$ ) into the medium [1,13,23], where  $l^*$  is the distance for photon momentum randomization. Similarly, the light collected by the detectors—in our case, each pixel of a camera—is modeled as that given by a diffusion model at points located  $l^*$  into the medium. We derive  $f_i$  using the extrapolated zero-flux boundary conditions shown in Fig. 2 to simulate an infinite homogeneous slab geometry [1]. The extrapolated boundary condition can accommodate mismatched background refractive indices at the surface. We set the extrapolated boundary  $l_s = 5.03D$  away from the physical surface, analogous to an interface between air and scatterers in water [43] and useful in our earlier experiments [23], to approximately model the physical boundary for the experimental results that we present. Four pairs of excitation and fluorescent image sources are placed to approximately enforce  $\phi = 0$  at the extrapolated boundary. Superposition of the physical and image sources allows analytic expressions for  $g_x(\mathbf{r}_s, \mathbf{r}_f)$  and  $g_m(\mathbf{r}_f, \mathbf{r}_i)$  to be obtained that have the form given in Eq. (3).

### B. Position estimation

If a fluorescent inhomogeneity is present, which can be determined subject to some probability of detection [23], in order to localize it we must estimate  $\mathbf{r}_f$ . This can be accomplished through minimization of the cost function

$$c(\mathbf{r}_f) = \min_w \|\mathbf{y} - w\mathbf{f}(\mathbf{r}_f)\|_{\Upsilon^{-1}}^2, \quad (6)$$

over all  $\mathbf{r}_f$  of interest, where  $\mathbf{y}$  is a vector of  $N$  measurements,  $\mathbf{f}(\mathbf{r}_f)$  is a vector of  $N$  forward calculations  $f_i(\mathbf{r}_f)$ , from Eq. (5),  $\Upsilon = \alpha \text{diag}[|y_1|, \dots, |y_N|]$  is the noise covariance matrix, for which we assume a Gaussian noise model characterized by  $\alpha$  [13], a constant determined by the modulation depth and the physical characteristics of the detector, and for an arbitrary vector  $\mathbf{v}$ ,  $\|\mathbf{v}\|_{\Upsilon^{-1}}^2 = \mathbf{v}^H \Upsilon^{-1} \mathbf{v}$ , where  $H$  denotes the Hermitian transpose. A two-step procedure can be used to solve this optimization problem [23,40,44], where the minimization in Eq. (6) with respect to  $w$  leads to

$$\tilde{w}(\mathbf{r}_f) = \frac{\mathbf{f}^T(\mathbf{r}_f) \Upsilon^{-1} \mathbf{y}}{\mathbf{f}^T(\mathbf{r}_f) \Upsilon^{-1} \mathbf{f}(\mathbf{r}_f)}, \quad (7)$$

found by taking the derivative with respect to  $w$  and setting the result equal to zero, and this estimate results in the modified cost function

$$c(\mathbf{r}_f) = \|\mathbf{y} - \tilde{w}(\mathbf{r}_f) \mathbf{f}(\mathbf{r}_f)\|_{\Upsilon^{-1}}^2. \quad (8)$$

The maximum likelihood estimates are then

$$\hat{\mathbf{r}}_f = \arg \min_{\mathbf{r}_f} c(\mathbf{r}_f), \quad (9)$$

$$\hat{w} = \tilde{w}(\hat{\mathbf{r}}_f), \quad (10)$$

where Eq. (8) is minimized over a set of values for  $\mathbf{r}_f$  bounded by the slab geometry. Therefore, the estimate  $\hat{\mathbf{r}}_f$  in Eq. (9) is the position within the slab that returns the lowest value of the cost function given in Eq. (8). In our illustrative example of a homogeneous scattering slab, this minimization can be computed quickly because the Green's functions from Eq. (4) used to calculate  $\mathbf{f}(\mathbf{r}_f)$  are closed-form and given by Eq. (3). However, the forward model data could also be generated using finite-element or related numerical methods [42], at the cost of increased computational time.

### C. Noise model

A Gaussian noise model is implied by Eq. (6) and the use of nonzero elements only on the diagonal of  $\Upsilon$  is a consequence of the assumption of independent measurements. The model assumes that each measurement is normally distributed with a mean equal to the noiseless measurement and a variance that is proportional to the dc ( $\omega = 0$ ) component of the noiseless measurement [13]. Simulated noisy data can therefore be numerically generated as

$$\text{Re}[y_i] = \text{Re}[\tilde{f}_i(\mathbf{r}_f)] + [\alpha |\tilde{f}_i(\mathbf{r}_f)|]^{1/2} N(0, 1), \quad (11)$$

$$\text{Im}[y_i] = \text{Im}[\tilde{f}_i(\mathbf{r}_f)] + [\alpha |\tilde{f}_i(\mathbf{r}_f)|]^{1/2} N(0, 1), \quad (12)$$

where  $N(0, 1)$  is a zero-mean Gaussian random variable with unit variance. The signal-to-noise ratio (SNR, in dB)



at the  $i$ th detector is then

$$\text{SNR}_i = 10 \log_{10} \left( \frac{1}{\alpha} |\tilde{f}_i(\mathbf{r}_f)| \right). \quad (13)$$

This noise model assumes that the uncertainty in the estimated position of the fluorescent inhomogeneity ( $\hat{\mathbf{r}}_f$ ) is dominated by measurement noise. This would not be the case, for example, if the fluorophores changed position or diffused significantly during the integration time of the measurement [45,46].

## IV. RESULTS

### A. Simulation and localization uncertainty

We first generate 50 noisy independent measurements for an assumed 30 dB SNR using Eq. (11) (for  $\omega = 0$ ) to demonstrate the localization of a fluorescent inhomogeneity in a highly scattering slab. Figure 3 shows the geometry that we consider, where the positions of an excitation source, a fluorescent inhomogeneity (which is modeled as a point fluorescent source), and  $N = 400$  detectors are shown as red, green, and blue points, respectively. The true location of the fluorescent inhomogeneity is  $\mathbf{r}_{fi}$  and the slab is 18 mm thick, with  $\mu_a = 0$  and  $\mu'_s = 0.9 \text{ mm}^{-1}$ . A region of interest of size  $2 \times 2 \times 1.8 \text{ cm}^3$  is discretized into a 3D grid. Following the localization procedure of Sec. III. B,  $\tilde{w}(\mathbf{r}_f)$  from Eq. (7) and then  $c(\mathbf{r}_f)$  from Eq. (8) are evaluated at each grid point. Values for  $\hat{\mathbf{r}}_f$  and  $\hat{w}$  are then calculated using Eq. (9) and then Eq. (10). Example simulation results are presented in the Appendix, along with a multiresolution method that proves to be computationally efficient. We use this multiresolution approach to localize the fluorescent inhomogeneity and achieve SRDOI.

Because the measurements are noisy, each localized position  $\hat{\mathbf{r}}_f$  falls within an underlying probability distribution function  $p(\mathbf{r}_f)$ , with mean  $\mu$  and standard deviation  $\sigma$ . The performance of the localization can therefore be

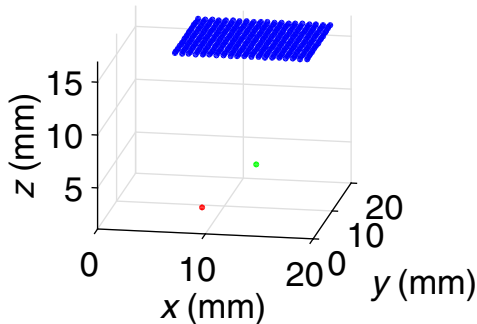


FIG. 3. The slab problem geometry with  $\mathbf{r}_s = (8.09, 9.07, 1.11)$  mm plotted as the red point,  $\mathbf{r}_{fi} = (12.77, 10.79, 5.0)$  mm plotted as the green point, and  $N = 400$  detector locations  $\mathbf{r}_i$  plotted as blue points. These positions are used so that the simulation and experimental results can be compared. The slab has the same dimensions (18 mm thick) and properties as used in the experiment.

evaluated by estimating  $\sigma$ , the localization uncertainty [45–47]. By the central limit theorem,  $\sigma$  can be estimated from a sufficient number of samples of  $p(\mathbf{r}_f)$  [48]. Therefore,  $\hat{\sigma}_x$ ,  $\hat{\sigma}_y$ , and  $\hat{\sigma}_z$  can be calculated, which are the estimates of  $\sigma$  corresponding to each of the  $(x, y, z)$  coordinates of  $\mathbf{r}_f$ . The same geometry, optical properties,  $\mathbf{r}_s$ ,  $\mathbf{r}_i$ , and  $\mathbf{r}_f$  as in Fig. 3 are used to obtain numerical samples of  $p(\mathbf{r}_f)$  as follows. Each simulated measurement data set is used to determine  $\hat{\mathbf{r}}_f$ , using Eq. (9) with multiresolution. Then,  $\hat{\sigma}_x$ ,  $\hat{\sigma}_y$ , and  $\hat{\sigma}_z$  are calculated from 50 values of  $\hat{\mathbf{r}}_f$ . The results of this statistical analysis are shown in Fig. 4. The detector plane is located  $3D$  into the top of the medium ( $z = 18 - 3D$  mm). The depth of the fluorescent inhomogeneity, or its distance below the top surface, is 13 mm, as shown in Fig. 3. Figure 4(a) gives plots of  $\hat{\sigma}_x$ ,  $\hat{\sigma}_y$ , and  $\hat{\sigma}_z$  versus SNR, and Fig. 4(b) shows a subset of this data as ellipses, where the major and minor axes have dimension  $4\hat{\sigma}_x$  or  $4\hat{\sigma}_y$ . We choose  $4\hat{\sigma}_x$  and  $4\hat{\sigma}_y$  to indicate the space containing 95% of the localized points. Figure 4(c) presents plots of  $\hat{\sigma}_x$ ,  $\hat{\sigma}_y$ , and  $\hat{\sigma}_z$  versus depth for a constant SNR of 30 dB, and Fig. 4(d) shows plots of ellipses for different depths. It is clear that  $\hat{\sigma}_z$  is consistently larger than  $\hat{\sigma}_x$  and  $\hat{\sigma}_y$ . This occurs because the detectors are on a constant  $z$  plane. The value of  $\hat{\sigma}_z$  could be reduced to the levels of  $\hat{\sigma}_x$  and  $\hat{\sigma}_y$  by placing additional detectors in the  $x$ - $z$  or  $y$ - $z$  planes. Thus,  $\hat{\sigma}_x$  and  $\hat{\sigma}_y$  are better indicators of the achievable localization uncertainty for the geometry in Fig. 3. The reason why  $\hat{\sigma}_x$  does not equal  $\hat{\sigma}_y$  and the ellipses are not perfect circles may be due to only 50 samples being used or the fact that the detector locations are not symmetric with respect to the inhomogeneity. We note that even though we use the same equation for the forward model that is used to generate the simulated data, it is not guaranteed that the localization will work due to the addition of simulated noise. In the next section, we will validate our localization scheme with experimental data and demonstrate that the simulated results closely match those from the experiment.

### B. Experiment

We present the results of an experimental study of the accuracy of SRDOI with measurement data collected using the arrangement shown in Fig. 5(a). A highly scattering slab of thickness  $d = 18$  mm is created by stacking three pieces of white plastic (Cryo Industries, Acrylite FF; a clear acrylic with 50 nm  $\text{TiO}_2$  scatterers) with dimensions  $140 \times 140 \times 6 \text{ mm}^3$ . A hole with a diameter of 1 mm and a depth of 2 mm is drilled into the top center of the bottom slab. The size of this hole is large relative to the expected localization uncertainty; however, it is small enough to be well approximated by a fluorescent point source in a heavily scattering medium [23]. A 10 mM stock of the fluorophore Maleimide ATTO 647N (peak  $\lambda_x = 646$  nm, peak  $\lambda_m = 664$  nm) in dimethyl sulfoxide (DMSO)

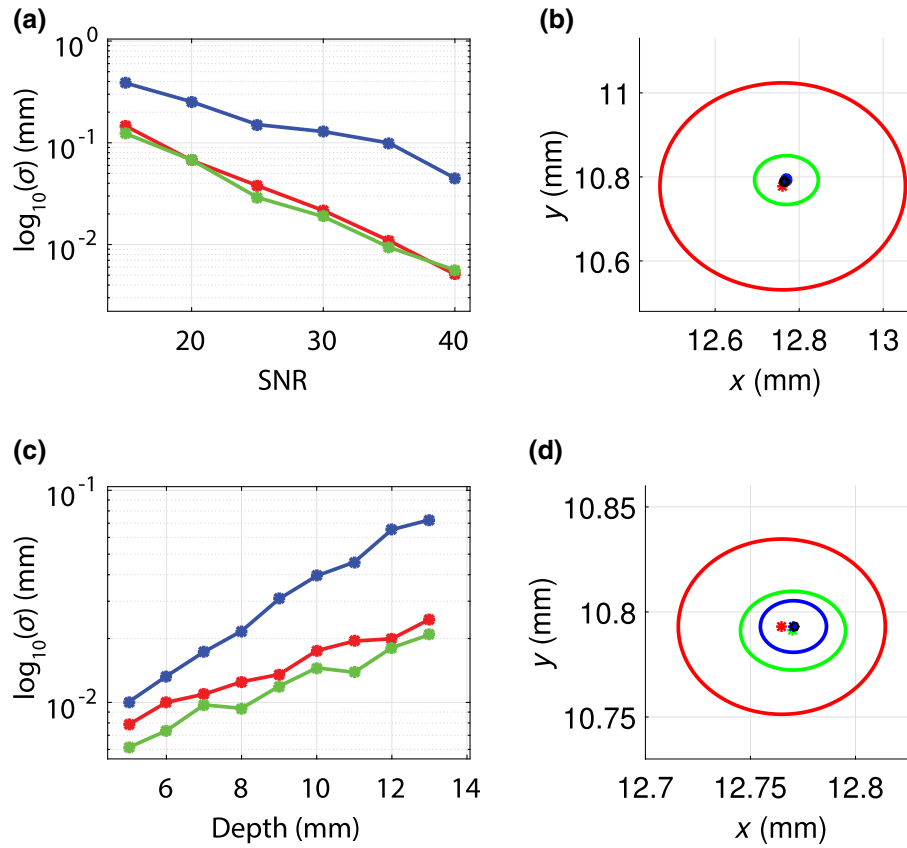


FIG. 4. Uncertainty in the numerical localization of a fluorescent inhomogeneity in the slab geometry shown in Fig. 3. The standard deviations are estimated using 50 noisy independent measurements that are generated using Eqs. (11) and (12). (a) A plot of the standard deviation of the localization distribution in each direction,  $\hat{\sigma}_x$ ,  $\hat{\sigma}_y$ , and  $\hat{\sigma}_z$  versus the SNR, plotted as red, green, and blue curves, respectively. The depth of the fluorescent inhomogeneity is 13 mm, as shown in Fig. 3.  $\hat{\sigma}_z$  is larger than  $\hat{\sigma}_x$  and  $\hat{\sigma}_y$  because the detectors are only in the  $x$ - $y$  plane. (b) Plots of the localization distribution ellipses in the  $x$ - $y$  plane with major and minor axes of lengths  $4\hat{\sigma}_x$  or  $4\hat{\sigma}_y$  and means given by their center points. Red, green, and blue ellipses correspond to SNRs of 15, 25, and 40 dB, respectively. (c) The localization distribution standard deviations,  $\hat{\sigma}_x$ ,  $\hat{\sigma}_y$ , and  $\hat{\sigma}_z$  versus depth, plotted as red, green, and blue curves, respectively, with a 30 dB SNR. (d) The localization distribution ellipses in the  $x$ - $y$  plane with major and minor axes of length  $4\hat{\sigma}_x$  or  $4\hat{\sigma}_y$  and means given by their center points. Red, green, and blue ellipses correspond to depths of 13, 8, and 5 mm, respectively. This shows that uncertainty increases as depth increases.

is used to prepare a 10  $\mu$ M diluted solution of the fluorophore. This fluorophore solution is carefully placed into the drilled hole in the bottom highly scattering slab, using a pipette, and a needle allows removal of the air bubbles.

The filtered output of a pulsed supercontinuum source (EXR-20 NKT Photonics, 5 ps seed pulse width, 20 MHz repetition rate, VARIA tunable filter) was used to generate the excitation light at  $\lambda_x = 633$  nm with a 10 nm bandwidth, as shown in Fig. 5(a). With this bandwidth, the average excitation power is approximately 15 mW. Measurements at  $\lambda_m = 676$  nm are made through an OD6 bandpass filter having a bandwidth of 29 nm (Edmund Optics 86-996), to reject the excitation light. Measurements at  $\lambda_x$  are performed by removing the bandpass filter. All measurements are pseudo-CW [corresponding to unmodulated light data and  $\omega = 0$  in Eqs. (1) and (2)], with the CCD camera (PIMAX,  $512 \times 512$  pixels) integration

time being long compared to the pulsed laser repetition rate (20 MHz). A  $\lambda_x$  measurement result with an integration time of 30 ms is shown in Fig. 5(b).

All  $\lambda_m$  measurements are calibrated by subtracting corresponding measurements of the filter bleed-through, according to  $y_i = y_i^{\text{slab}} - y_i^{\text{bleed}}$ , where  $y_i$  is the  $i$ th component of  $\mathbf{y}$ ,  $y_i^{\text{slab}}$  is the  $i$ th experimental datum captured from the slab, and  $y_i^{\text{bleed}}$  is the  $i$ th experimental datum from the slab without the fluorescent inhomogeneity present. A calibrated  $\lambda_m$  measurement with an integration time of 1 s is shown in Fig. 5(c). We select  $N = 400$  detector locations (pixels) around the maximum value, as shown by the blue dots. The values (indicated by the color bar) at these positions are used to construct the data vector  $\mathbf{y}$  in Eq. (6).

In order to calculate the forward solution in Eq. (4),  $\mu'_s$ ,  $\mu'_a$  and  $\mathbf{r}_i$  for each detector along with  $\mathbf{r}_s$ , must be known. To determine these, first the positions of all pixels in

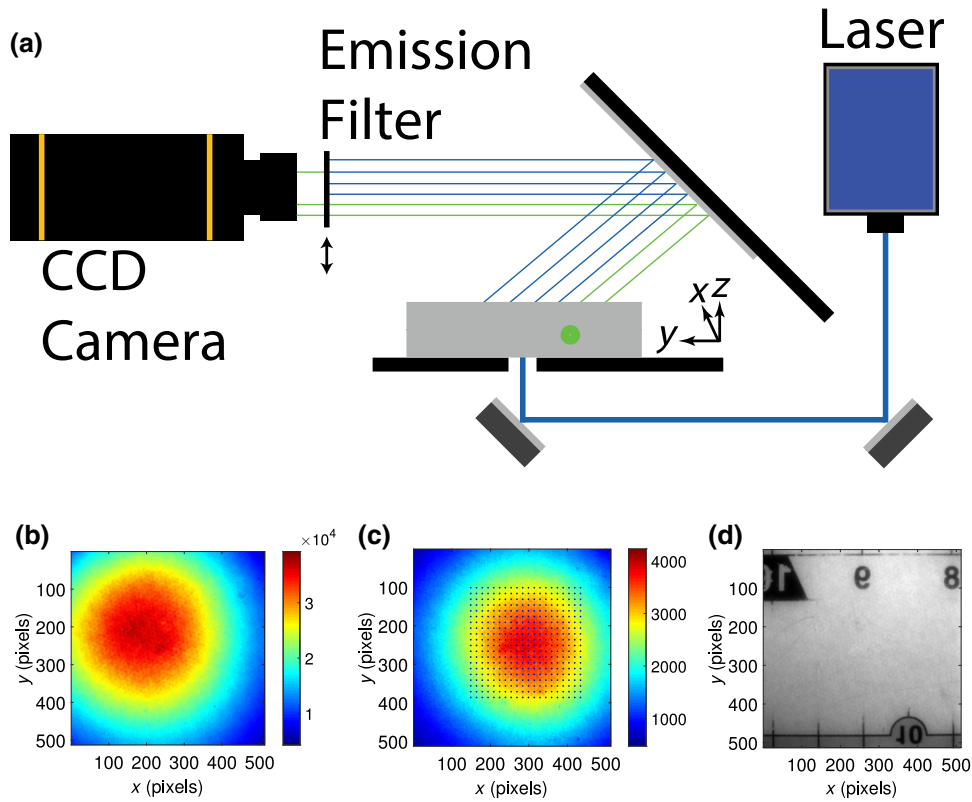


FIG. 5. (a) The experimental setup for localization of a fluorescent inhomogeneity (green point). The fluorescent inhomogeneity (ATTO 647N) is embedded in a highly scattering slab that is 18 mm thick. The laser source is a filtered pulsed supercontinuum source (EXR-20 NKT Photonics, 5 ps seed pulse width, 20 MHz repetition rate, VARIA tunable filter). The laser source is tuned to  $\lambda_x$  and detection is by a CCD camera with or without a bandpass filter at  $\lambda_m$ . (b) Light at  $\lambda_x$  detected by the CCD camera without the bandpass filter. The excitation light must be attenuated by  $10^6$  using a bandpass filter in order to measure the fluorescent emission, therefore the fluorescent signal is considered to be negligible. (c) Light at  $\lambda_m$  (after background subtraction) detected by the CCD camera with the bandpass filter. The positions of the 400 detectors are shown as blue dots. (d) A CCD image of a ruler, showing the field of view (about  $22.02 \times 22.02 \text{ mm}^2$ ). Images of the ruler are used to convert pixels to millimeters.

Figs. 5(b) and 5(c) are found in millimeters, using images of a ruler like that shown in Fig. 5(d). Care is taken in the alignment of the experimental components so that the distance between each detector point in the  $x$  and  $y$  dimensions is approximately the same (0.043 mm). The  $x_i$  and  $y_i$  coordinates of the vector  $\mathbf{r}_i$  can then be determined from the positions of the chosen 400 detector points and the  $z$  coordinate is  $(18 - 3D)$  mm, to satisfy the zero-flux boundary condition at the top of the scattering medium [1]. The point directly below the maximum intensity in Fig. 5(b) indicates the source position,  $\mathbf{r}_s$ . This position of maximum intensity is estimated by fitting a two-dimensional (2D) Gaussian function [45] to Fig. 5(b). This procedure results in  $\mathbf{r}_s = (8.09, 9.07, 3D)$  mm, where the  $z$  component is  $3D$  to satisfy the boundary condition at the bottom of the scattering medium [1]. The 2D Gaussian fit is also used to estimate the true location of the fluorescent inhomogeneity using a data set with 50 times the integration time of that used for Fig. 5(c), resulting in a much higher SNR than that of Fig. 5(c). The true location is estimated as the centroid with coordinates  $\mathbf{r}_{ft} = (12.77, 10.79, 5.0)$  mm,

where the  $z$  component at the center of the drilled hole is found from the thickness of the white plastic slabs (6 mm) and the depth of the drilled hole (2 mm). We note that the 2D Gaussian fit does not provide depth information, motivating the use of the localization method in Sec. III even in this simple example.

The optical parameters of the slab,  $\mu'_s$  and  $\mu_a$ , estimated by fitting  $g_x(\mathbf{r}_s, \mathbf{r}_i)$  to the data, shown in Fig. 5(b), where in this case,  $\mathbf{r}' = \mathbf{r}_s$ ,  $\mathbf{r} = \mathbf{r}_i$ , and the  $z$  components of  $\mathbf{r}_s$  and  $\mathbf{r}_i$  depend on  $\mu'_s$  and  $\mu_a$ . The data in Fig. 5(b) are captured with the fluorescent inhomogeneity present, but because the bandpass filter used in the experiment attenuates the excitation light by a factor of  $10^6$ , the fluorescent signal in Fig. 5(b) is assumed to be negligible compared to the transmitted excitation light. It is also assumed that the scattering medium background exists throughout the small volume occupied by the fluorophore. The scattering slabs used have very low absorption in the wavelength range for these experiments, so we set  $\mu_a = 0$ . The estimated  $\mu'_s$  of the slab (at 633 nm) is found to be  $0.9 \text{ mm}^{-1}$ , giving  $3D = 1.11 \text{ mm}$ . These values are within the

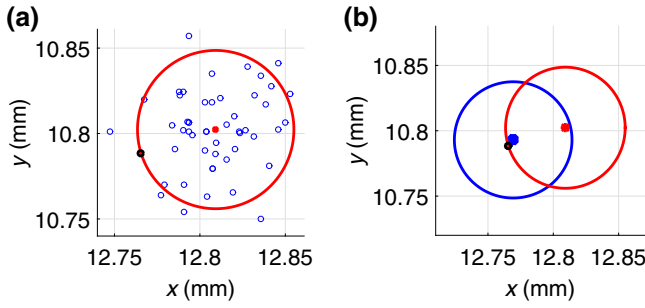


FIG. 6. The experimental localization uncertainty for the fluorescent inhomogeneity embedded in the highly scattering slab of Fig. 5. Experimental values for  $\hat{\sigma}_x$ ,  $\hat{\sigma}_y$ , and  $\hat{\sigma}_z$  are estimated using 50 independent experimental measurements. (a) A plot of the  $(x,y)$  components of the localized positions as blue points. These points are used to calculate the major and minor axes of the red ellipse, which has dimensions  $4\hat{\sigma}_x$  or  $4\hat{\sigma}_y$ , as well as its center red point, which is the mean. The black point is the true location that is estimated with a 2D Gaussian fit. (b) Comparison of the experimental uncertainty to the numerical uncertainty. The blue ellipse is generated from numerical data with mean SNR = 28.9 dB to match the experimental value and the red ellipse is the same as in (a). See Table I for the numerical values.

uncertainty of previous estimates using the same method [49]. The positions  $\mathbf{r}_s$ ,  $\mathbf{r}_i$ , and  $\mathbf{r}_{fi}$ , are those indicated in Fig. 3, and are used for the corresponding numerical simulations in the Appendix and Fig. 4, so that the simulation and experimental results can be compared.

The forward solution calculated in Eq. (4) using the experimental parameters, along with the experimental measurement vector  $\mathbf{y}$ , allow localization of the fluorescent inhomogeneity embedded in the highly scattering slab. In order to characterize the experimental localization uncertainty, the  $\lambda_m$  measurement shown in Fig. 5(c) is repeated 50 times. Localization using these 50 measurements then allows calculation of the experimental  $\hat{\sigma}_x$ ,  $\hat{\sigma}_y$ , and  $\hat{\sigma}_z$ . The resulting values are shown plotted as an ellipse in Fig. 6(a), with an axial ratio of  $\hat{\sigma}_y/\hat{\sigma}_x = 0.0232/0.0229$  (i.e., close to circular), and presented in Table I.

In order to validate the SRDOI method, the experimental results in Fig. 6(a) can be compared to the numerical data in Fig. 4. These results are all generated using the same  $\mathbf{r}_s$ ,  $\mathbf{r}_i$ , and  $\mathbf{r}_{fi}$ , and identical scattering medium optical parameters,  $\mu'_s$  and  $D$ . In order to estimate the SNR of the experiment, we calculate the ML estimate of the noise

parameter  $\alpha$  from the full form of Eq. (6) [50], giving

$$\hat{\alpha} = \frac{1}{N} \|\mathbf{y} - \hat{\mathbf{w}}\mathbf{f}(\hat{\mathbf{r}}_f)\|_{\tilde{\mathbf{Y}}^{-1}}^2, \quad (14)$$

where  $\tilde{\mathbf{Y}} = \text{diag}[|y_1|, \dots, |y_N|]$  uses measured data. The SNR of the  $i$ th detector is then estimated, using Eq. (13), as

$$\text{SNR}_i = 10 \log_{10} \left( \frac{1}{\hat{\alpha}} |\hat{\mathbf{w}}_i \mathbf{f}_i(\hat{\mathbf{r}}_f)| \right). \quad (15)$$

The SNR is calculated for all 400 detectors, using Eq. (15) and one of the 50 experimental data sets and its corresponding values for  $\hat{\mathbf{w}}$  and  $\hat{\mathbf{r}}_f$ . The mean experimental SNR is found to be 28.9 dB, its standard deviation across detectors is 0.62 dB, and its maximum is 29.9 dB. We use this mean SNR to generate the blue ellipse in Fig. 6(b), which is plotted with the red ellipse from Fig. 6(a). The values for the numerical localization uncertainties are also presented in Table I. Note that the experimental and numerical uncertainties are close, signifying that Eq. (13) describes the noise process well. The difference between the experimental mean and the true location is likely due to the fit approximation used to determine the true location and estimation error.

### C. Resolution

A natural way to compare the localization uncertainties to the resolution of diffuse optical imaging is to calculate the FWHM of the density function  $p(\mathbf{r}_f)$  that describes the localized positions. For a localization uncertainty  $\sigma_i$ , corresponding to the spatial components of  $\sigma$ , and a Gaussian spread of localized points, we can write the resolution as

$$\text{Resolution} = 2\sqrt{2 \ln 2} \sigma_i \approx 2.36\sigma_i, \quad (16)$$

corresponding to the FWHM. The numerical and experimental results are summarized in Table I for the case of depth = 13 mm, as shown in Fig. 3, and a mean SNR of 28.9 dB, found for the experiment. The  $\hat{\mu}_x$ ,  $\hat{\mu}_y$ , and  $\hat{\mu}_z$  are the mean of the localized position components. The FDOT resolution is estimated as half the depth.

## V. DISCUSSION

In this work, we develop a localization method that allows imaging of fluorescent inhomogeneities deep in

TABLE I. Estimated numerical and experimental localization uncertainties, means, and the resulting resolution (mm). The resolution of FDOT is assumed to be half the depth.

	SRDOI numerical	SRDOI experimental	FDOT
$(\hat{\sigma}_x, \hat{\sigma}_y, \hat{\sigma}_z)$	(0.0225, 0.0222, 0.1301)	(0.0229, 0.0232, 0.1089)	—
$(\hat{\mu}_x, \hat{\mu}_y, \hat{\mu}_z)$	(12.769, 10.793, 4.972)	(12.809, 10.802, 4.875)	—
Resolution	(0.0530, 0.0523, 0.3064)	(0.0539, 0.0546, 0.2564)	6.5



heavily scattering media with unprecedented spatial resolution. The method is validated numerically and experimentally, demonstrating an improvement of two orders of magnitude in resolution compared to DOI. An analytic forward solution in an infinite slab geometry is used, but analytic solutions could be derived for arbitrary geometries using the Kirchhoff approximation [41]. Alternatively, numerical methods such as the finite-element method could be used to solve the forward problem for inhomogeneous media, where DOT could be employed to determine  $\mu'_s$  and  $\mu_a$  [51,52]. However, the limited resolution to which  $\mu'_s$  and  $\mu_a$  could be estimated with DOT in inhomogeneous media might increase the localization uncertainty. The localization constraints could be incorporated into the FDOT framework [17,53], potentially allowing reconstruction of superresolution images. Also, Eq. (6) could be minimized using alternative optimization methods, such as a gradient search.

The diffusion model presented in Eqs. (1) and (2) assumes that the photon current density does not change over one transport mean free path,  $l^* = 3D$ . For the white plastic slab used here,  $l^* = 1.11$  mm at 633 nm, which is much larger than the localization uncertainties in Table I. Therefore, SRDOI can find a fluorescent inhomogeneity with a resolution that is much less than the minimum length described by the physics in the diffusion model. This is possible because of the prior information that has been incorporated into the localization. The results suggest that the localization uncertainty is dominated by measurement noise and not inaccuracies in the model. Therefore, a more accurate model, such as the radiative transfer equation (RTE), is not required unless the combination of the diffusion equation forward model and the prior information is insufficient for accurate localization. This could be the case with weak scatter or high absorption, for example.

We find that a single excitation source position,  $\mathbf{r}_s$ , is sufficient for the situation considered, which is practical for experimentation. However, multiple excitation source positions or expanded beam excitation may increase the fluorescence emission and reduce the localization uncertainty. A low-pass spatial filter could be applied to the experimental data before estimating  $\mathbf{r}_f$  in order to further reduce the localization uncertainty (results not shown). This would smooth the noisy experimental data prior to the localization. The computational time could be reduced and the experiment simplified by using fewer detectors [23]. A few sensitive photodetectors placed at the surface of a scattering medium should be sufficient to localize an inhomogeneity with higher SNR than can be achieved with a CCD camera. Figure 5(a) shows a transmission measurement, but a reflection measurement could be performed. Also, the localization uncertainty may be reduced through the use of modulated light (nonzero  $\omega$ ). For *in vivo* applications, longer wavelengths may improve the SNR due to lower light absorption in tissue.

Practical application of SRDOI requires access to fluorescent light data that can be assumed to originate from single fluorescent inhomogeneities. This could be accomplished through known variations in space, time, the fluorescence emission spectrum, or a combination of these. Variation in space could simply be fluorescent inhomogeneities separated by distances greater than the FWHM of the PSF. Variation in time could be a unique temporal delay for each inhomogeneity, where measurements with short integration times (and sufficient SNR) could allow separation of the temporal responses. Finally, if each inhomogeneity emits photons at different energies, a spectral measurement can allow separation of each response. All of these variations are possible with blinking quantum dots of different diameters [54], where each quantum dot can then be localized in deep tissue.

Localization techniques have also been developed in microscopy for improving resolution [55,56]. For example, in stochastic optical reconstruction microscopy (STORM) [57], a subset of fluorescent molecules that are separated by a distance greater than the diffraction limit are switched between fluorescent and nonfluorescent states. Each molecule is then located with an uncertainty that is much less than the diffraction limit. With multiple measurements, a superresolution image is formed by combining many localized positions. However, this is a fundamentally different class of problem, in which scatter is largely ignored and the imaging system objective function is incorporated into the localization framework. In our case, a model for the heavily scattering domain is used in an optimization-based localization framework. Interestingly, the improvement in spatial resolution that is achieved with superresolution in microscopy is comparable to that achieved by SRDOI. For example, a diffraction-limited resolution of 200 nm is improved to a few nanometers when imaging single fluorescent molecules [58], an improvement of about two orders in magnitude.

The localization technique presented here enables superresolution imaging in other physical imaging problems that use forward models, such as photoacoustic tomography [59], electrical impedance tomography [60], seismic waveform tomography [61], and microwave imaging [62]. While the experiments differ, the premise that we present should apply.

One potential application of SRDOI is brain imaging [63–65]. Signaling between neurons is accompanied by an increase in the local concentration of calcium, which can modulate the emission of fluorophores within the brain [66,67]. Each neuron can be treated as a fluorescent inhomogeneity that, for example, emits photons when the neuron fires. In this case, measurements by a CCD camera or a fiber array with an appropriate integration time could provide data from individual neurons to allow each neuron or a set of neurons to be localized. In principle, this could provide an image of a whole animal brain or the

brain surface *in vivo* at a resolution of tens of micrometers. These images would provide information on how the brain encodes perceived information into chemical and electrical neural activity, and how local neural circuits interact with different areas of the brain. Correlation maps with such data should prove useful for studying neurological diseases and developing treatments [68].

## VI. CONCLUSION

In this work, we introduce a diffuse optical imaging modality where the positions of inhomogeneities embedded in highly scattering tissue-like media are estimated in order to achieve high spatial resolution through localization. Examples of inhomogeneities include biological structures such as cells that are stained with targeted fluorescent contrast agents. Therefore, the SRDOI localization approach enables designed fluorescent studies of biochemical processes in deep tissue and *in vivo*. Alternatively, absorbing inhomogeneities that do not fluoresce could be localized [40,44]. We demonstrate the capability of SRDOI numerically and experimentally by localizing a fluorescent inhomogeneity at a depth of 13 mm in a highly scattering slab. The localization uncertainty is characterized in order to understand the limits to which the location of the inhomogeneity can be estimated. From this uncertainty, we find that SRDOI can achieve a spatial resolution better than tens of microns, an improvement of over two orders of magnitude compared to DOI methods such as FDOT. This superresolution optical imaging method has a potential for deep *in vivo* imaging and can be applied to a broad class of physical problems that use forward models, addressing a critical need in biomedical imaging for deep-tissue high-resolution optical imaging.

## ACKNOWLEDGMENTS

This work was funded in part by the National Science Foundation (Grant Nos. CISE-1218909 and CISE-1618908) and the National Institutes of Health (Grant No. 1R21CA182235-01A1). This paper describes objective technical results and analysis. Any subjective views or opinions that might be expressed in the paper do not necessarily represent the views of the U.S. Department of Energy or the United States Government. We thank Daniel Ysselstein for preparing the ATTO647N sample.

## APPENDIX: LOCALIZATION WITH A MULTIREOLUTION APPROACH

In this Appendix, simulation examples of the localization methods used to generate the results are presented. Consider a region of interest of size  $2 \times 2 \times 1.8 \text{ cm}^3$ , as defined in Sec. IV A. The localization procedure described in Sec. III B is performed on the discretized region of interest with  $N_x = 17$  points in the  $x$  dimension,  $N_y = 17$

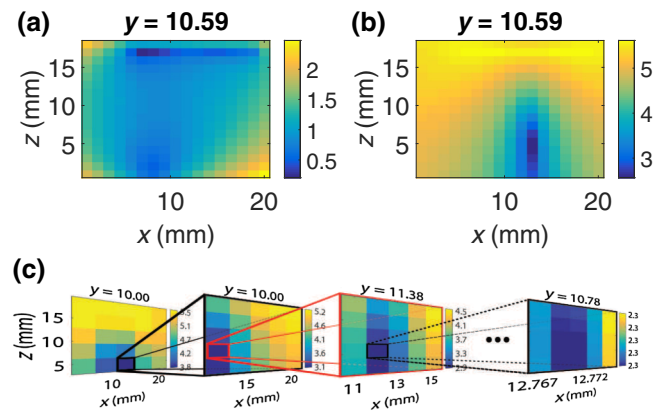


FIG. 7. The numerical localization of a point fluorescent inhomogeneity embedded in a highly scattering slab with the same dimensions and properties as used in the experiment. The slab problem geometry is illustrated in Fig. 3. Measurements are simulated using Eq. (4) with  $w = 10$  and a 30 dB SNR, and  $\tilde{w}(\mathbf{r}_f)$  from Eq. (7) and  $c(\mathbf{r}_f)$  from Eq. (8) are evaluated over the region of interest with dimensions  $2 \times 2 \times 1.8 \text{ cm}^3$ . (a) Plot of  $\tilde{w}(\mathbf{r}_f)$  slice and (b) plot of  $c(\mathbf{r}_f)$  slice for fixed  $y$  calculated from a grid of  $N_x = N_y = N_z = 17$ , such that the plots contain the point that minimizes  $c(\mathbf{r}_f)$ . The values of fixed  $y$  (mm) are shown above the plots and the color bars have log scales with arbitrary units. Using Eq. (9),  $\hat{\mathbf{r}}_f = (12.94, 10.59, 5.29)$ , and using Eq. (10),  $\hat{w} = 10.07$ . The localization errors in the  $x$ ,  $y$ , and  $z$  dimensions are 1.37%, 1.85%, and 5.88%, respectively. The coarse discretization of the region of interest is a primary contributor to the estimation error. (c) Localization with multiresolution. Cost is calculated and minimized in the region of interest with the same dimension as before, but with a grid of  $N_x = N_y = N_z = 5$ . Plots of  $c(\mathbf{r}_f)$  slices for fixed  $y$  are shown for multiresolution iterations 1, 2, 3, and 13. At iteration 13, from Eq. (9),  $\hat{\mathbf{r}}_f = (12.77, 10.78, 4.98)$ , and from Eq. (10),  $\hat{w} = 10.02$ . The localization errors in the  $x$ ,  $y$ , and  $z$  dimensions are 0.05%, 0.05%, and 0.19%, respectively.

points in the  $y$  dimension, and  $N_z = 17$  points in the  $z$  dimension. Figures 7(a) and 7(b) show plots of  $\tilde{w}(\mathbf{r}_f)$  and  $c(\mathbf{r}_f)$  for a fixed  $y$  such that the plots contain the minimum of  $c(\mathbf{r}_f)$ . The estimated location of the fluorescent point source  $\hat{\mathbf{r}}_f$  can then be determined. The localization error is calculated as  $[(\mathbf{r}_{fl} - \hat{\mathbf{r}}_f)/\mathbf{r}_{fl} \times 100]\%$ , and the error in Figs. 7(a) and 7(b) is relatively high because of the discretization of the spatial grid over the region of interest.

In order to achieve high resolution, the grid spacing of the points within the region of interest must be reduced from that used in Figs. 7(a) and 7(b). However, this presents a computational problem when evaluating  $\tilde{w}(\mathbf{r}_f)$  and  $c(\mathbf{r}_f)$ , because Eq. (4) must be calculated for each combination of  $\mathbf{r}_i$  and  $\mathbf{r}_f$  within the region of interest. For this reason, we apply a multiresolution method to simultaneously reduce the computational time and the discretization error of the localization. This multiresolution approach is similar to multigrid in the general sense that it incorporates a hierarchy of discretization grids into the localization

[50,69,70]. However, multigrid algorithms propagate solutions back and forth between coarse and fine grids to reduce errors, whereas our multiresolution approach iterates strictly in one direction, from coarse to finer grids. Therefore, we use the term multiresolution to describe the method, as demonstrated in Fig. 7(c). First, the cost  $c(\mathbf{r}_f)$  is calculated and minimized in the region of interest with dimensions  $2 \times 2 \times 1.8 \text{ cm}^3$ , as before, but with a grid of  $N_x = N_y = N_z = 5$ . The cost is then iteratively calculated on successively smaller regions of interest, each of which encompasses the point of minimum cost found from the previous iteration. At each iteration after the first, the region of interest extends a distance equal to the grid spacing of the previous iteration along each dimension, around the point of minimum cost, and the grid contains the same number of grid points ( $5 \times 5 \times 5$ ). This procedure is repeated until convergence, which we define as two grids where the change in the minimum cost is less than 0.1%, but not equal to zero. In Fig. 7(c), the first three iterations are shown. It is observed that successive iterations appear to close in on the point of lowest cost. After 13 iterations, the convergence condition is satisfied and  $\hat{\mathbf{r}}_f$  is calculated using Eq. (9). The localization error is much less than that of Figs. 7(a) and 7(b), because multiresolution effectively minimizes the discretization error. Multiresolution is important in achieving the results in Sec. IV because it substantially reduces computational times.

- 
- [1] Michael S. Patterson, Britton Chance, and Brian C. Wilson, Time resolved reflectance and transmittance for the non-invasive measurement of tissue optical properties, *Ann. Phys.* **28**, 2331 (1989).
- [2] M. A. OLeary, D. A. Boas, B. Chance, and A. G. Yodh, Refraction of Diffuse Photon Density Waves, *Phys. Rev. Lett.* **69**, 2658 (1992).
- [3] A. P. Gibson, J. C. Hebden, and Simon R. Arridge, Recent advances in diffuse optical imaging, *Phys. Med. Biol.* **50**, R1 (2005).
- [4] Ernst Abbe, Beiträge zur theorie des Mikroskops und der mikroskopischen Wahrnehmung, *Arch. Mikr. Anat.* **9**, 413 (1873).
- [5] Roarke Horstmeyer, Haowen Ruan, and Changhui Yang, Guide-star-assisted wavefront-shaping methods for focusing light into biological tissue, *Nat. Photon.* **9**, 563 (2015).
- [6] S. M. Popoff, G. Lerosey, R. Carminati, M. Fink, A. C. Boccarda, and S. Gigan, Measuring the Transmission Matrix in Optics: An Approach to the Study and Control of Light Propagation in Disordered Media, *Phys. Rev. Lett.* **104**, 100601 (2010).
- [7] Matthieu Davy, Zhou Shi, and Azriel Z. Genack, Focusing through random media: Eigenchannel participation number and intensity correlation, *Phys. Rev. B* **85**, 035105 (2012).
- [8] Thomas Chaigne, Jérôme Gateau, Ori Katz, Emmanuel Bossy, and Sylvain Gigan, Light focusing and two-dimensional imaging through scattering media using the photoacoustic transmission matrix with an ultrasound array, *Opt. Lett.* **39**, 2664 (2014).
- [9] Jason A. Newman and Kevin J. Webb, Imaging Optical Fields Through Heavily Scattering Media, *Phys. Rev. Lett.* **113**, 263903 (2014).
- [10] Jason A. Newman, Qiaoen Luo, and Kevin J. Webb, Imaging Hidden Objects with Spatial Speckle Intensity Correlations over Object Position, *Phys. Rev. Lett.* **116**, 073902 (2016).
- [11] C. P. Gonatas, Masaru Ishii, John S. Leigh, and John C. Schotland, Optical diffusion imaging using a direct inversion method, *Phys. Rev. E* **52**, 4361 (1995).
- [12] Jorge Ripoll, Ralf B. Schulz, and Vasilis Ntziachristos, Free-Space Propagation of Diffuse Light: Theory and Experiments, *Phys. Rev. Lett.* **91**, 103901 (2003).
- [13] J. C. Ye, K. J. Webb, C. A. Bouman, and R. P. Millane, Optical diffusion tomography by iterative coordinate descent optimization in a Bayesian framework, *J. Opt. Soc. Am. A* **16**, 2400 (1999).
- [14] David L. Everitt, S. P. Wei, and X. D. Zhu, Analysis and optimization of a diffuse photon optical tomography of turbid media, *Phys. Rev. E* **62**, 2924 (2000).
- [15] Vadim A. Markel and John C. Schotland, Symmetries, inversion formulas, and image reconstruction for optical tomography, *Phys. Rev. E* **70**, 056616 (2004).
- [16] Vasilis Ntziachristos and Ralph Weissleder, Charge-coupled-device based scanner for tomography of fluorescent near-infrared probes in turbid media, *Med. Phys.* **29**, 803 (2002).
- [17] A. B. Milstein, S. Oh, K. J. Webb, C. A. Bouman, Q. Zhang, D. A. Boas, and R. P. Millane, Fluorescence optical diffusion tomography, *Appl. Opt.* **42**, 3081 (2003).
- [18] Esther H. R. Tsai, Brian Z. Bentz, Venkatesh Chelvam, Vaibhav Gaid, Kevin J. Webb, and Philip S. Low, *In vivo* mouse fluorescence imaging for folate-targeted delivery and release kinetics, *Biomed. Opt. Express* **5**, 2662 (2014).
- [19] Wouter Peelaerts, Luc Bousset, Anke Van der Perren, Anastacia Moskalyuk, Rocco Pulizzi, Michele Giugliano, Chris Van den Haute, Ronald Melki, and Veerle Baekelandt,  $\alpha$ -synuclein strains cause distinct synucleinopathies after local and systemic administration, *Nature* **522**, 340 (2015).
- [20] Vasilis Ntziachristos, Jorge Ripoll, Lihong V. Wang, and Ralph Weissleder, Looking and listening to light: The evolution of whole-body photonic imaging, *Nat. Biotechnol.* **23**, 313 (2005).
- [21] Edward L. Hull, Michael G. Nichols, and Thomas H. Foster, Localization of luminescent inhomogeneities in turbid media with spatially resolved measurements of CW diffuse luminescence emittance, *Appl. Opt.* **37**, 2755 (1998).
- [22] Marcus Pfister and Bernhard Scholz, Localization of fluorescence spots with space-space MUSIC for mammography-like measurement systems, *J. Biomed. Opt.* **9**, 481 (2004).
- [23] Adam B. Milstein, Michael D. Kennedy, Philip S. Low, Charles A. Bouman, and Kevin J. Webb, Statistical approach for detection and localization of a fluorescing mouse tumor in Intralipid, *Appl. Opt.* **44**, 2300 (2005).
- [24] Jean-Pierre L'Huillier and Fabrice Vaudelle, Improved localization of hidden fluorescent objects in highly



- scattering slab media based on a two-way transmittance determination, *Opt. Exp.* **14**, 12915 (2006).
- [25] Y. Chen, G. Zheng, Z. H. Zhang, D. Blessington, M. Zhang, H. Li, Q. Liu, L. Zhou, X. Intes, S. Achilefu, and B. Chance, Metabolism-enhanced tumor localization by fluorescence imaging: *In vivo* animal studies, *Opt. Lett.* **28**, 2070 (2003).
- [26] X. D. Li, M. A. O’Leary, D. A. Boas, Britton Chance, and A. G. Yodh, Fluorescent diffuse photon density waves in homogeneous and heterogeneous turbid media: Analytic solutions and applications, *Appl. Opt.* **35**, 3746 (1996).
- [27] J. Ripoll, M. Nieto-Vesperinas, and Rémi Carminati, Spatial resolution of diffuse photon density waves, *J. Opt. Soc. Am. A* **16**, 1466 (1999).
- [28] Brian W. Pogue, Troy O. McBride, Ulf L. Osterberg, and Keith D. Paulsen, Comparison of imaging geometries for diffuse optical tomography of tissue, *Opt. Exp.* **4**, 270 (1999).
- [29] D. A. Boas, K. Chen, D. Grebert, and M. A. Franceschini, Improving the diffuse optical imaging spatial resolution of the cerebral hemodynamic response to brain activation in humans, *Opt. Lett.* **29**, 1506 (2004).
- [30] Lingling Zhao, Vivian K. Lee, Seung-Schik Yoo, Guohao Dai, and Xavier Intes, The integration of 3-D cell printing and mesoscopic fluorescence molecular tomography of vascular constructs within thick hydrogel scaffolds, *Biomaterials* **33**, 5325 (2012).
- [31] Edward E. Graves, Jorge Ripoll, Ralph Weissleder, and Vasilis Ntziachristos, A submillimeter resolution fluorescence molecular imaging system for small animal imaging, *Med. Phys.* **30**, 901 (2003).
- [32] Samuel Bélanger, Maxime Abran, Xavier Intes, Christian Casanova, and Frederic Lesage, Real-time diffuse optical tomography based on structured illumination, *J. Biomed. Opt.* **15**, 016006 (2010).
- [33] Guy Satat, Barmak Heshmat, Dan Raviv, and Ramesh Raskar, All photons imaging through volumetric scattering, *Sci. Rep.* **6**, 33946 (2016).
- [34] Xiaoqing Zhou, Ying Fan, Qiang Hou, Huijuan Zhao, and Feng Gao, Spatial-frequency-compression scheme for diffuse optical tomography with dense sampling data set, *Appl. Opt.* **52**, 1779 (2013).
- [35] J. A. Moon, R. Mahon, M. D. Duncan, and J. Reintjes, Resolution limits for imaging through turbid media with diffuse light, *Opt. Lett.* **18**, 1591 (1993).
- [36] X. D. Li, T. Durduran, A. G. Yodh, B. Chance, and D. N. Pattanayak, Diffraction tomography for biochemical imaging with diffuse-photon density waves, *Opt. Lett.* **22**, 573 (1997).
- [37] A. H. Gandjbakhche, R. Nossal, and R. F. Bonner, Resolution limits for optical transillumination of abnormalities deeply embedded in tissues, *Med. Phys.* **21**, 185 (1994).
- [38] Brian W. Pogue and Keith D. Paulsen, High-resolution near-infrared tomographic imaging simulations of the rat cranium by use of *a priori* magnetic resonance imaging structural information, *Opt. Lett.* **23**, 1716 (1998).
- [39] Vasilis Ntziachristos, A. G. Yodh, Mitchell D. Schnall, and Britton Chance, MRI-guided diffuse optical spectroscopy of malignant and benign breast lesions, *Neoplasia* **4**, 347 (2002).
- [40] Brian Z. Bentz, Timothy C. Wu, Vaibhav Gaiind, and Kevin J. Webb, Diffuse optical localization of blood vessels and 3D printing for guiding oral surgery, *Appl. Opt.* **56**, 6649 (2017).
- [41] Jorge Ripoll, Vasilis Ntziachristos, Remi Carminati, and Manuel Nieto-Vesperinas, Kirchhoff approximation for diffusive waves, *Phys. Rev. E* **64**, 051917 (2001).
- [42] Martin Schweiger and Simon Arridge, The Toast ++ software suite for forward and inverse modeling in optical tomography, *J. Biomed. Opt.* **19**, 040801 (2014).
- [43] Richard C. Haskell, Lars O. Svaasand, Tsong-Tseh Tsay, Ti-Chen Feng, Bruce J. Tromberg, and Matthew S. McAdams, Boundary conditions for the diffusion equation in radiative transfer, *J. Opt. Soc. Am. A* **11**, 2727 (1994).
- [44] Guangzhi Cao, Vaibhav Gaiind, Charles A. Bouman, and Kevin J. Webb, Localization of an absorbing inhomogeneity in a scattering medium in a statistical framework, *Opt. Lett.* **32**, 3026 (2007).
- [45] Russell E. Thompson, Daniel R. Larson, and Watt W. Webb, Precise nanometer localization analysis for individual fluorescent probes, *Biophys. J.* **82**, 2775 (2002).
- [46] Xavier Michalet, Mean square displacement analysis of single-particle trajectories with localization error: Brownian motion in an isotropic medium, *Phys. Rev. E* **82**, 041914 (2010).
- [47] Francisco Balzarotti, Yvan Eilers, Klaus C. Gwosch, Arvid H. Gynn, Volker Westphal, Fernando D. Stefani, Johan Elf, and Stefan W. Hell, Nanometer resolution imaging and tracking of fluorescent molecules with minimal photon fluxes, *Science* **355**, 606 (2017).
- [48] Athanasios Papoulis and S. Unnikrishna Pillai, *Probability, Random Variables, and Stochastic Processes* (Tata McGraw-Hill Education, Boston, 2002).
- [49] Charles A. Thompson, Kevin J. Webb, and Andrew M. Weiner, Diffusive media characterization with laser speckle, *Appl. Opt.* **36**, 3726 (1997).
- [50] Jong Chul Ye, Charles A. Bouman, Kevin J. Webb, and Rick P. Millane, Nonlinear multigrid algorithms for Bayesian optical diffusion tomography, *IEEE Trans. Image Process.* **10**, 909 (2001).
- [51] Martin Schweiger, Simon R. Arridge, and David T. Delpy, Application of the finite-element method for the forward and inverse models in optical tomography, *J. Math. Imaging Vision* **3**, 263 (1993).
- [52] Jenni Heino, Simon Arridge, Jan Sikora, and Erkki Somersalo, Anisotropic effects in highly scattering media, *Phys. Rev. E* **68**, 031908 (2003).
- [53] Vivian Pera, Eric Zettergren, Dana H. Brooks, and Mark Niedre, Maximum likelihood tomographic reconstruction of extremely sparse solutions in diffuse fluorescence flow cytometry, *Opt. Lett.* **38**, 2357 (2013).
- [54] Ken T. Shimizu, Robert G. Neuhauser, Catherine A. Leatherdale, Stephen A. Empedocles, W. K. Woo, and Mounji G. Bawendi, Blinking statistics in single semiconductor nanocrystal quantum dots, *Phys. Rev. B* **63**, 205316 (2001).
- [55] Eric Betzig, George H. Patterson, Rachid Sougrat, O. Wolf Lindwasser, Scott Olenych, Juan S. Bonifacino, Michael W. Davidson, Jennifer Lippincott-Schwartz, and Harald F. Hess, Imaging intracellular fluorescent proteins at nanometer resolution, *Science* **313**, 1642 (2006).



- [56] Samuel T. Hess, Thanu P. K. Girirajan, and Michael D. Mason, Ultra-high resolution imaging by fluorescence photoactivation localization microscopy, *Biophys. J.* **91**, 4258 (2006).
- [57] Michael J. Rust, Mark Bates, and Xiaowei Zhuang, Sub-diffraction-limit imaging by stochastic optical reconstruction microscopy (storm), *Nat. Meth.* **3**, 793 (2006).
- [58] Hans Blom and Jerker Widengren, Stimulated emission depletion microscopy, *Chem. Rev.* **117**, 7377 (2017).
- [59] Minghua Xu and Lihong V. Wang, Universal back-projection algorithm for photoacoustic computed tomography, *Phys. Rev. E* **71**, 016706 (2005).
- [60] Margaret Cheney, David Isaacson, and Jonathan C. Newell, Electrical impedance tomography, *SIAM Rev.* **41**, 85 (1999).
- [61] R. Gerhard Pratt, Seismic waveform inversion in the frequency domain, part 1: Theory and verification in a physical scale model, *Geophysics* **64**, 888 (1999).
- [62] Tonny Rubk, Paul M. Meaney, Peter Meincke, and Keith D. Paulsen, Nonlinear microwave imaging for breast-cancer screening using Gauss-Newton's method and the CGLS inversion algorithm, *IEEE Trans. Antennas Propag.* **55**, 2320 (2007).
- [63] Michael Scherg, Functional imaging and localization of electromagnetic brain activity, *Brain Topogr.* **5**, 103 (1992).
- [64] Robert Prevedel, Young-Gyu Yoon, Maximilian Hoffmann, Nikita Pak, Gordon Wetzstein, Saul Kato, Tina Schrödel, Ramesh Raskar, Manuel Zimmer, Edward S. Boyden, and Alipasha Vaziri, Simultaneous whole-animal 3D imaging of neuronal activity using light-field microscopy, *Nat. Meth.* **11**, 727 (2014).
- [65] Adam T. Eggebrecht, Silvina L. Ferradal, Amy Robichaux-Viehoever, Mahlega S. Hassanpour, Hamid Dehghani, Abraham Z. Snyder, Tamara Hershey, and Joseph P. Culver, Mapping distributed brain function and networks with diffuse optical tomography, *Nat. Photon.* **8**, 448 (2014).
- [66] Ryohei Yasuda, Esther A. Nimchinsky, Volker Scheuss, Thomas A. Pologruo, Thomas G. Oertner, Bernardo L. Sabatini, and Karel Svoboda, Imaging calcium concentration dynamics in small neuronal compartments, *Sci. STKE* **2004**, 15 (2004).
- [67] Michael Lawrence Castanares, Vini Gautam, Jack Drury, Hans Bachor, and Vincent R. Daria, Efficient multi-site two-photon functional imaging of neuronal circuits, *Biomed. Opt. Express* **7**, 5325 (2016).
- [68] Ed Bullmore and Olaf Sporns, Complex brain networks: Graph theoretical analysis of structural and functional systems, *Nat. Rev. Neurosci.* **10**, 186 (2009).
- [69] A. Brandt, *Multigrid Techniques: 1984 Guide, with Applications to Fluid Dynamics* (GMD-Studien, Sankt Augustin, Germany, 1984).
- [70] Seungseok Oh, Charles A. Bouman, and Kevin J. Webb, Multigrid tomographic inversion with variable resolution data and image spaces, *IEEE Trans. Image Process.* **15**, 2805 (2006).